Vortex breakdown in swirling pipe flow of fluids with shear-dependent viscosity

Thomas O. Thornhill,[1] Tom Petit,[2] Robert J. Poole,[1] and David J.C. Dennis[1, a]

[1] *School of Engineering, University of Liverpool, Liverpool L69 3GH, UK*

[2] *DEN-Service d'Etudes des Matériaux Irradiés, CEA, Université Paris-Saclay, F-91191, Gif-sur-Yvette, France*

(Dated: 31 October 2018)

Laminar pipe flow with a controllable wall swirl has been studied both numerically and experimentally to explore the behaviour of inelastic shear-dependent fluids. The pipe consists of two smoothly joined sections that can be rotated independently about the same axis. The circumstance of flow entering a stationary pipe from a rotating pipe (decaying swirl) has been investigated. Numerical parametric studies using both a power-law model and a simplified Carreau model are conducted to investigate the effect of shear-thinning and shear-thickening on the flow structure and the critical swirl ratio required to induce the breakdown at a range of Reynolds numbers. A new method of scaling (i.e. a new Reynolds number) is presented that accounts for the shear-dependent viscosity. Using this Reynolds number the data for all fluids (shear-thickening, Newtonian and shear-thinning) approximately collapses. Experimental visualisations using an aqueous solution of a xantham gum confirm the conclusions drawn from the numerical results.

I. INTRODUCTION

Vortex breakdown of swirling flows – the formation of a stagnation point upstream of a region of near-stagnant recirculating flow – has fascinated and intrigued many since its discovery nearly 60 years ago[1–4]. One of the key reasons for such continued study is surely the inherent artistic beauty embedded within it (coupled with the non-trivial fluid dynamics at play). Classic flow visualisation text books[5] contain numerous such examples: experiments[6] and numerical simulations[7] of vortex breakdown in a rotating endwall cylindrical container; experiments[5] and numerical simulations[8] of vortex breakdown on delta wings, as well as supersonic flows[9]. Other examples of such visualisations can be found in papers studying cylindrical divergent tubes[10,11] and slit-tube arrangements[12] amongst many other flows. The flow also has many practical applications, the most widespread use being for flame stabilization in furnaces and combustion chambers where the recirculation bubble acts as a fluid-dynamical flame holder[2,3]. However, in some flows, vortex breakdown needs to be mitigated or avoided[13] and an improved understanding of the conditions leading to vortex breakdown is also important in this context.

A. Vortex breakdown in non-Newtonian fluids

The flow produced by rotating one of the end-walls in a cylindrical container completely filled with fluid is one of the few situations of vortex breakdown that has been studied in some detail for non-Newtonian fluids. It was first investigated by Böhme, Rubart & Stenger (1992)[14] using an essentially inelastic, shear-thinning fluid (0.1%

wt. carboxymethlcellulose in a water/glycerine mixture). The experimental study revealed single, double or triple breakdown bubbles that were quantitatively similar to those seen in the Newtonian case[6], although they did not occur at precisely the same Reynolds numbers (Re) and aspect ratios. Böhme, Rubart & Stenger (1992)[14] also conducted complimentary finite-element simulations that were found to be in reasonable agreement with the experimental findings. However, a study in the same geometry by Day et al. (1996)[15] found that the flow field for their non-Newtonian fluid was quite different to the Newtonian case. The important difference here being that the fluid was elastic (as well as shear-thinning) and it was at low Reynolds numbers and high elasticity numbers ($El = De/Re$, where De is the Deborah number) where elasticity becomes important and the behaviour was found to be very different to the Newtonian case. Indeed, at higher Reynolds numbers ($Re > 1.5$), and low El where the effects of elasticity were negligible, the flow reverted back to the steady, Newtonian-like flow pattern[15].

In further work in exactly the same facility as the benchmark Newtonian case[6], Escudier & Cullen (1996)[16] investigated the behaviour of strongly shear-thinning (pseudoplastic) fluids (which were only mildly elastic). They discovered flow regimes involving a double-vortex structure that was unlike the Newtonian case[6], or the previous non-Newtonian experiments using slightly shear-thinning[14] or highly elastic[15] fluids. Later, Stokes et al. (2001)[17,18] conducted a detailed experimental study of the flow of viscoelastic Boger fluids of various types and concentrations. They found that the critical conditions required for vortex breakdown varied significantly depending on the fluid used. Similar to Day et al. (1996)[15], they found that a Newtonian-like vortex breakdown occurred when inertia dominated, but weakly elastic fluids were found to have a stabilising effect and limit the range of conditions at which vortex breakdown was seen to occur[17]. However, when elastic effects dominated a

a)Electronic mail: djcd@liverpool.ac.uk

new time-dependent elastic instability (quite different to the Newtonian instability) was observed[18].

Rusak & Tichy (2002)[19] explored the effect of elasticity on the critical swirl level required for vortex breakdown to occur in a pipe flow of non-Newtonian fluid by performing a stability analysis utilising an Oldroyd-B constitutive model (representing a constant-viscosity Boger fluid) in the governing equations. It was found that increasing the relaxation time increases the critical swirl required for vortex breakdown to occur and also affected the size of the recirculation.

Other flows of non-Newtonian fluids in scenarios where vortex breakdown occurs have been studied, for example the flow between two rotating spheres[20]. The generation of vortex rings in shear-thinning fluids has also been investigated[21]. However, to date, the effect of shear-thinning fluids on vortex breakdown in swirling pipe flow has not received significant attention.

B. Vortex breakdown in swirling pipe flow

Vortex breakdown in swirling pipe flow was recently investigated experimentally and numerically using a Newtonian fluid by Dennis, Seraudie & Poole (2014)[22]. This work utilised a set-up that can be traced to the analytical and numerical work of Lavan et al (1969)[23], where the pipe consists of two smoothly joined sections that can be rotated independently about the same axis. Lavan et al[23] combined a linearised analytical solution with a finite-difference numerical technique. Subsequently, Macdonald (1991)[24] also took an analytical approach to reach a very similar prediction for the occurrence of vortex breakdown in this arrangement. Crane and Burley (1976)[25] conducted a further numerical investigation, as did Silvester et al (1986)[26]: both studies found broad agreement with the original work of Lavan et al. However, there was still no experimental validation of these predictions.

Columnar swirling flow in a pipe was investigated by Wang & Rusak (1997)[27] using the unsteady Euler equations. Their analysis showed that when the incoming flow has a swirl level that is above a critical level, the columnar flow becomes unstable and small axisymmetric disturbances propagate upstream and evolve into large disturbances that lead to the formation of a new state involving a recirculation region, i.e. vortex breakdown. Subsequently, numerical computations were performed that supported this mechanism of vortex breakdown[28].

Dennis, Seraudie & Poole (2014)[22] provided the first experimental results along with an updated numerical investigation. The agreement between the experimental visualisations and the numerical solutions was found to be excellent: both in terms of the size and structure of recirculation region and the critical conditions required to induce the vortex breakdown in this set-up. An example of the experimental visualistion and corresponding numerical simulation is shown in figure 1. It was observed that the recirculation region was steady and stationary
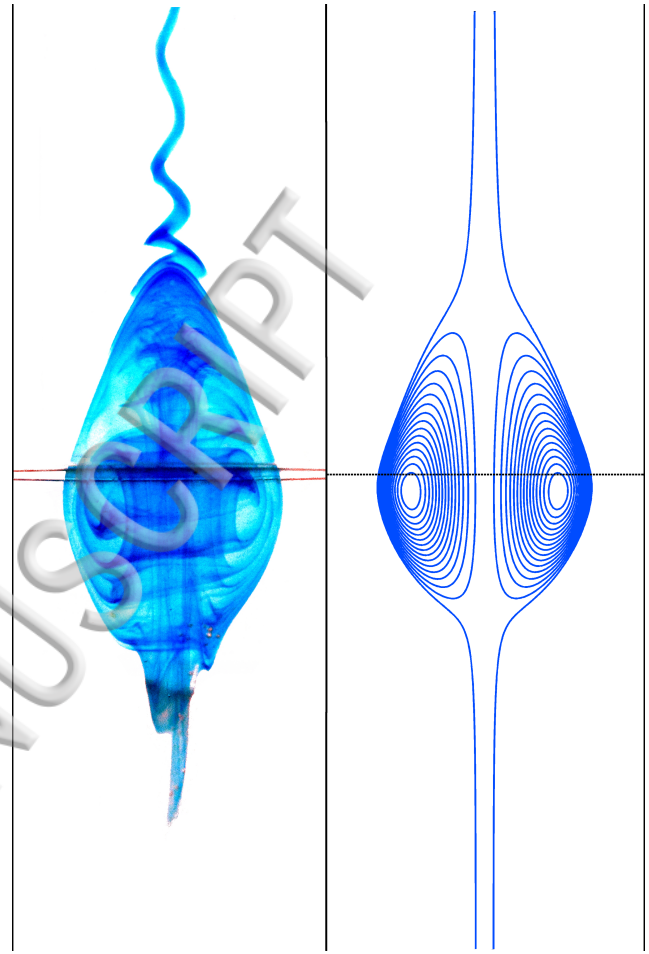
for constant boundary conditions.

FIG. 1: An illustrative example of vortex breakdown in swirling pipe flow with decaying swirl (upstream pipe rotation) $Re = 8$, $\Gamma = 15$; left hand side experiment; right hand side simulation. Bulk flow is from top to bottom. Reproduced from Phys. Fluids 26, 053602 (2014)[22], with the permission of AIP Publishing.

The flow is governed by two non-dimensional groups: the axial Reynolds number ($Re = \rho U D/\mu$, where U is the bulk velocity, D is the pipe diameter and μ the dynamic viscosity), and the swirl ratio ($\Gamma = 0.5\omega D/U$ where $0.5\omega D$ is the tangential velocity at the pipe wall). For a given Re, a certain swirl ratio is required in order to induce vortex breakdown. This is defined as the critical swirl ratio (Γ_c). The analytical solutions[23,24] accurately predicted this critical swirl ratio at vanishingly small Reynolds numbers ($Re < 1$), but broke down at higher Re. The numerical and experimental results showed that as Re increased Γ_c tended to a constant value[22]. As the swirl ratio is increased beyond the critical value the axial length of the recirculation region is seen to increase (particularly in the upstream direction, but also downstream)[22,26]. Very long recirculation re-

gions (several pipe diameters in length) could be created at high Γ. The radial width of the recirculation region also grew with increasing swirl ratio, but beyond a moderate value of Γ further growth was severely restricted by the confines of the geometry.

Two different cases have been investigated using the set-up. The first is *decaying swirl*, which is where the upstream pipe is rotated and the downstream pipe is stationary, thus the swirl in the flow decays downstream of the pipe join. The second situation is *growing swirl*, and is the opposite: the upstream pipe is stationary and downstream pipe is rotated, therefore the swirl in the flow grows downstream of the pipe join. In the case of decaying swirl, vortex breakdown was seen to occur on the pipe axis whereas in the growing-swirl case vortex breakdown occurred at the tube wall and a toroidal zone of recirculation was observed[22].

Overall, the previous work has demonstrated that the occurrence of vortex breakdown, as well as the size and shape of the resulting recirculation region, can be controlled by the speed of wall rotation and the choice of wall rotated. This indicates that wall rotation could be utilised as a flow control device in industrial applications. Many viscous liquids used in processing and manufacturing are non-Newtonian and thus far no non-Newtonian fluid properties have been investigated in this geometry. In this paper we do this by experimentally studying the behaviour of an essentially inelastic shear-thinning solution for the case of decaying swirl. We use the experimental results to validate a Generalised Newtonian Fluid (the simple power-law) model, as well as a simplified Carreau model, using comparative numerical solutions and subsequently extend the use of these models across a wide range of shear-thinning and shear-thickening behaviour not accessible with the experiment.

II. EXPERIMENT

A. Experimental arrangement

A full description (including schematic) of the experimental rig used to perform all the experiments in this work can be found in Dennis, Seraudie & Poole (2014)[22]. Briefly, it consists of two identical glass pipes with an internal diameter $D = 50$mm that are aligned end-on in a vertical orientation. Each of the two pipes are $13D$ in length. A small gap (< 1mm) between the two pipes that make up the working section enables the two pipes to be rotated independently. Surrounding this junction, the pipes are enclosed in a glass viewing box filled with the working fluid, which removes distortion due to the curvature of the pipe wall for the purposes of imaging the flow visualisation. The rotational speed of each pipe can be controlled to an accuracy of ± 2rpm, with a maximum rotation rate of 400rpm, providing access to a wide range of swirl ratios. The flow is gravity-driven from a supply tank situated at the top of the system. This system approximates to a constant head tank as the volume of fluid and surface area of the tank are large compared to the flow rate through the test pipes. To control the throughput, two needle valves are located downstream of the working section with a float style mass flow meter installed between them to monitor the flow rate. The mass flow meter is regularly calibrated across the operational range of the experiment against weight measurements of the working fluid that has passed through the rig over a certain time period (the order of a few minutes).

B. Working fluids

Approximately 40 litres of fluid is required to fill the system. In this investigation we use a semi-dilute aqueous solution of xanthan gum (Keltrol TF from Kelco). The molecular weight is quoted by the manufacturer as being approximately 10^6g/mol. At the concentrations of xanthan gum (C_{XG}) used in this investigation (0.1% to 0.15% w/w) the solution is shear-thinning and its rigid-rod-like structure means that, outside of the linear small amplitude regime, it is largely inelastic[29–32]. This fluid has been chosen because of its shear-thinning nature and low normal stress elasticity allowing us to attempt to isolate the non-Newtonian effects. This enables us to use it to compare to simulations in which we model shear-thinning effects, but not viscoelasticity. The effect of viscoelasticity on vortex breakdown in this flow geometry is not considered in this work and will be the subject of future investigations.

The density and temperature of the xanthan gum mixtures were measured before and after each set of experiments using an Anton Paar DMA 35N density meter (with a quoted accuracy of 0.001g/cm^3 and 0.2°C). Indicative values are $\rho = 997$kg/m^3 at 23.5°C. The viscosity of the mixture was measured using a TA Instruments Rheolyst AR 1000 N controlled-stress rheometer in conjunction with a 60mm diameter 2° acrylic cone to within an uncertainty of 2%[33]. Example rheological measurements showing the relationship between shear rate and shear viscosity for three concentrations of xanthan gum are given in figure 2. The corresponding power-law and Carreau-Yasuda fits are also shown in figure 2 with the model parameters given in tables I and II respectively. It is noted that the infinite shear rate viscosity for the Carreau-Yasuda fits are below that of the solvent, which is physically impossible. This is due to the lack of rheological measurements at very high shear rates (which means that μ_∞ is not accurately modelled). However, as these shear rates are not reached in the flow being studied it is not crucial.

As expected, the measured rheology of the mixture only follows a power-law over a limited range of shear rates. The range where the fit is reasonable corresponds to $\approx 3 - 300$s^{-1}, which is also approximately the range of wall shear rates we expect in the rotating pipe experiment. The Carreau-Yasuda fits do not require a limited

TABLE I: Power-law model variables used to fit the measured rheology.

Model number	C_{XG}	Model variables	
		$k(\text{Pa.s}^n)$	n_{PL}
PL 1	0.10	0.09	0.58
PL 2	0.12	0.13	0.55
PL 3	0.15	0.23	0.46

TABLE II: Carreau-Yasuda model variables used to fit the measured rheology.

Model number	C_{XG}	Model variables				
		$\mu_0(\text{Pa.s})$	$\mu_\infty(\text{Pa.s})$	$\lambda(\text{s})$	a	n_{CY}
CY 1	0.10	0.221	0.000400	5.26	0.693	0.492
CY 2	0.12	0.510	0.00224	1.84	0.387	0.696
CY 3	0.15	1.89	0.0029	3.50	0.342	0.804

range of shear rates due to their asymptotic nature. This allows the fits to follow the measured rheology of the mixture reasonably at all values of shear rate.

Estimating the critical overlap concentration c^* from the intrinsic viscosity $[\eta]$ determined from capillary u-tube viscometer measurements gives $c^* \approx 1/[\eta] \approx$ 530ppm. Extensional rheology measurements could not be obtained for the xanthan gum at these concentrations using the CaBER technique, presumably as a consequence of its rigid structure and therefore low Trouton ratios. Measurements of the first normal-stress difference for these fluids were also below the sensitivity of our TA rheometer and confirm the suggestion that the fluid is only weakly-elastic. This lack of data prevents the accurate determination of Deborah (De, based on the product of a non-linear relaxation time and an inverse timescale for the flow, i.e. the rotational speed of the pipe) or Weissenberg numbers (Wi, based on the product of non-linear relaxation time and a characteristic shear rate) for our fluid flows. However, based on estimates of the first normal stress differences measured for 0.25% xanthan gum[34], we would estimate maximum values on the order of 0.1 for both De and Wi confirming that we are probing shear-thinning effects alone largely unaffected by viscoelasticity. We note that all real fluids do contain some level of elasticity however.

III. NUMERICAL METHOD

To compute the flow field within the rotating pipe flow we make use of the fact that the flow is laminar, incompressible, steady and axisymmetric (i.e. two-dimensional). The governing equations are then those expressing conservation of mass (equation 1) and momentum (equation 2), where $\boldsymbol{u}$ represents the vector velocity, p the static pressure, ρ the fluid density and μ its
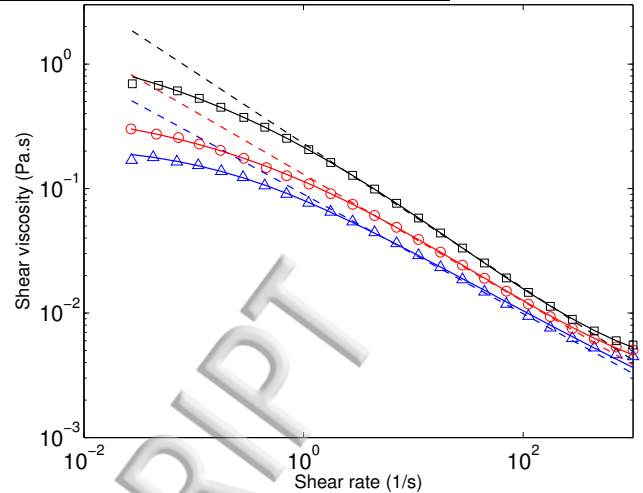

FIG. 2: Examples of rheological measurements (at 24°C) of the dependence of shear viscosity on shear rate for 0.10% xanthan gum (blue triangles) with PL 1 fit (blue dashed line) and CY 1 fit (blue continuous line); 0.12% xanthan gum (red circles) with PL 2 fit (red dashed line) and CY2 fit (red continuous line); and 0.15% xanthan gum (black squares) with PL 3 fit (black dashed line) and CY 3 fit (black continuous line)

dynamic viscosity.

$$\nabla \cdot \boldsymbol{u} = 0 \tag{1}$$

$$\rho \left(\boldsymbol{u} \cdot \nabla \boldsymbol{u} \right) = -\nabla p + \nabla \cdot \mu \nabla \boldsymbol{u} \tag{2}$$

The set-up of the numerical simulations follows the Newtonian work of Dennis, Seraudie & Poole (2014)[22] precisely, except for the implementation of the power-law model for viscosity. Here, we only outline the main aspects of the simulation and the reader is directed to that work for full details of the method and the mesh convergence study. The appropriate boundary conditions for this problem are axisymmetric conditions on the centre-line, fixed velocity conditions on the pipe walls, uniform flow velocity at the inlet far upstream of the junction and the outlet boundary condition far downstream of the junction. To ensure fully-developed flow at the junction, the length of each pipe (i.e. upstream and downstream of join) was set to 50 pipe radii[35]. We used Fluent (in ANSYS WorkBench 14.5) to solve Equations 1 and 2 subject to these boundary conditions. All calculations were carried out with a 80×3200 mesh (i.e. 256,000 cells) corresponding to mesh M3 from[22], which was found to provide grid independent results.

A. Power-law model

To simulate both non-Newtonian shear-thinning and shear-thickening behaviour we use a power-law model of

the form given in equation 3 where μ_{PL} is the dynamic viscosity of the fluid (units $Pa.s$), k is the flow consistency index ($kg \cdot s^{n-2}/m$), $\dot{\gamma}$ is a shear rate magnitude ($1/s$) and n_{PL} is the power law index.

$$\mu_{PL} = k\dot{\gamma}^{n_{PL}-1} \tag{3}$$

The amount of shear-thinning/thickening is defined by the power law index (n_{PL}) where $n_{PL} < 1$ for a shear-thinning fluid, $n_{PL} > 1$ for a shear-thickening fluid and $n_{PL} = 1$ for a Newtonian fluid. The larger the deviation from $n_{PL} = 1$ the more shear-thinning/thickening the fluid is. Minimum and maximum limits on the viscosity are imposed as 10^{-5}Pa.s and 10^5Pa.s respectively. We confirmed that the results are insensitive to further increases in these limits.

B. Carreau-Yasuda model

A Carreau-Yasuda model was also used to simulate non-Newtonian shear-thinning behaviour, allowing a direct comparison to be made between the Carreau-Yasuda and power-law models in relation to the experimental results. The Carreau-Yasuda model is given in equation 4 where μ_{CY} is the dynamic viscosity of the fluid, with μ_0 being the dynamic viscosity at zero shear rate and μ_∞ being the dynamic viscosity at infinite shear rate (units $Pa.s$), $\dot{\gamma}$ is a shear rate magnitude ($1/s$) and λ (s), a and n_{CY} are model parameters.

$$\mu_{CY} = \mu_\infty + \frac{\mu_0 - \mu_\infty}{\left(1 + (\lambda\dot{\gamma})^a\right)^{\frac{n_{CY}}{a}}} \tag{4}$$

The model is comprised of two constants (μ_0 and μ_∞) connected by a power-law where, a affects the shape of the transition region, λ is a time constant that determines where the change from constant to power-law occurs and n_{CY} describes the slope of the power-law. The amount of shear-thinning/thickening can then therefore be defined by the model parameter (n_{CY}) where $n_{CY} > 0$ for a shear-thinning fluid, $n_{CY} < 0$ for a shear-thickening fluid and $n_{CY} = 0$ for a Newtonian fluid. The larger the deviation from $n_{CY} = 0$ the more shear-thinning/thickening the fluid is.

C. Simplified Carreau model

To allow another direct comparison to the power-law model for a range of both shear-thinning/thickening fluids, without a fit to the measured rheology, a simplified Carreau model, of the form given in equation 5, was matched to the power-law, of the form given in equation 3. In this simplified Carreau model μ_{SC} is the dynamic viscosity of the fluid, with μ_0 being the dynamic viscosity at zero shear rate, $\dot{\gamma}$ is a shear rate magnitude ($1/s$) and λ_{SC} and n_{SC} are model parameters.

$$\mu_{SC} = \mu_0[1 + (\lambda_{SC}\dot{\gamma})^2]^{\frac{n_{SC}-1}{2}} \tag{5}$$

The matching procedure used to allow this comparison is stated by Escudier, Oliveira & Pinho (2002)[36]. The equations 6 and 7 show how the power-law and simplified Carreau models are related[36].

$$k = \mu_0(\lambda_{SC}^{n_{SC}-1}) \tag{6}$$

$$n_{SC} = n_{PL} \tag{7}$$

The models are matched such that the amount of shear-thinning/thickening for both models is defined by the power law index (n_{PL})[36]. For the results presented here, we have used $\mu_0 = 2$ Pa.s and $\lambda = 1$ s for all the simplified Carreau models. We have briefly tested the effect of Carreau number ($Cu = \lambda_{SC}\dot{\gamma}$)[30] and found that the Re trends we discuss are dominant over the effect of Carreau number for the fluids modelled. A comparison of the power-law and matched Carreau models is shown in figure 3. This demonstrates the agreement between the models in the power-law region, but a diversion as the simplified Carreau models asymptote to a constant (μ_0) at low shear rates, which is more representative of the real fluid rheology.
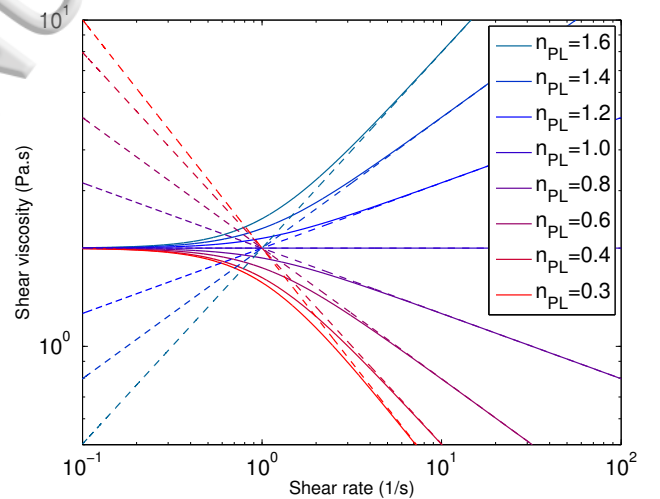

FIG. 3: Simplified Carreau models with corresponding matched power-law models (dashed lines) for power-law indices in the range 0.4–1.6.

IV. DEFINITION OF REYNOLDS NUMBER

For a Newtonian fluid flow through a pipe, the Reynolds number (Re) is given in equation 8. Calculation of Re is straightforward given the material properties of the fluid, the pipe geometry and the mass flow rate.

$$Re = \frac{\rho U D}{\mu} \tag{8}$$

For a non-Newtonian fluid, specifically a shear-thinning or shear-thickening fluid, the value of viscosity used to calculate Re is not straightforward as the viscosity varies throughout the flow field. Employing the power-law model described in section III A, the Reynolds number can be defined as in equation 9, which is a combination of equations 3 and 8;

$$Re = \frac{\rho U D}{k \dot{\gamma}^{n-1}}. \tag{9}$$

To compute this Re it is necessary to define a characteristic shear rate of the flow. For pipe flow this can be roughly estimated, based on scaling arguments and characteristic values, as the gradient of the axial velocity as given in equation 10, where r is radial coordinate and $R = D/2$ is the radius of the pipe:

$$\dot{\gamma} = \frac{dV_x}{dr} \approx \frac{U}{R}. \tag{10}$$

However, for the rotating pipe flow under consideration here there is an alternative definition based on the rotation rate of the pipe as given in equation 11,

$$\dot{\gamma} = \frac{dV_\theta}{dx} \approx \frac{\omega R}{R} = \omega, \tag{11}$$

where V_θ is the azimuthal velocity and ω is the rotational speed of the pipe. Here we are approximating the shear rate as the change in azimuthal velocity in the axial direction from $V_\theta \approx \omega R$ in the rotating (upstream) pipe to zero in the stationary (downstream) pipe over an axial distance of order R.

Given the estimates of these two shear rates in equations 10 and 11, and noting that the swirl ratio is defined as $\Gamma = \omega R/U$, it is clear that the shear rate based on rotation will be greater than the shear rate based on axial flow by a factor equivalent to the swirl ratio (Γ). As Γ is necessarily high in order for breakdown to occur, we might expect the shear rate based on rotation to be more relevant to the vortex breakdown phenomenon.

Using a characteristic shear-rate defined based on the axial flow (equation 10) the Reynolds number Re_x can be defined as,

$$Re_x = \frac{\rho U D}{k(U/R)^{n-1}} = \frac{2\rho U^{2-n} R^n}{k}. \tag{12}$$

Alternatively, using a characteristic shear-rate based on the rotational velocity (equation 11), the Reynolds number Re_ω can be defined as,

$$Re_\omega = \frac{\rho U D}{k\omega^{n-1}} = \frac{\rho U D}{k(U\Gamma/R)^{n-1}} = \frac{2\rho U^{2-n} R^n}{k} \Gamma^{1-n}. \tag{13}$$

Equations 12 and 13 show that these two Reynolds numbers (Re_x and Re_ω) are directly related to each other through the swirl ratio and the power-law index:

$$Re_x = Re_\omega \Gamma^{n-1}. \tag{14}$$

The definition of the Reynolds numbers presented above are only valid for the power-law model. The Carreau-Yasuda and simplified Carreau models require somewhat different Reynolds number expressions. This was done by using the same estimations for $\dot{\gamma}$ (shear rate magnitude) and procedure as presented above, giving equation 15 for the Carreau-Yasuda model,

$$Re_{x(CY)} = \frac{2\rho U R}{\mu_\infty + \frac{\mu_0 - \mu_\infty}{(1+(\lambda U/R)^a)^{n_{CY}/a}}} \tag{15}$$

and equations 16 and 17 for the simplified Carreau,

$$Re_{x(SC)} = \frac{2\rho U R}{\mu_0[1 + (\lambda_{SC}U/R)^2]^{\frac{n_{SC}-1}{2}}} \tag{16}$$

$$Re_{\omega(SC)} = \frac{2\rho U R}{\mu_0[1 + (\lambda_{SC}U\Gamma/R)^2]^{\frac{n_{SC}-1}{2}}}. \tag{17}$$

As we have two definitions of Re based on the two different estimates of shear-rate, we also have two different Carreau numbers for the simplified Carreau model as given in equations 18 and 19,

$$Cu_x = \lambda \frac{U}{R} \tag{18}$$

$$Cu_\omega = \lambda\omega. \tag{19}$$

V. COMPARISON OF EXPERIMENTAL AND NUMERICAL RESULTS FOR A SHEAR-THINNING FLUID

Experimental, numerical and analytical results for vortex breakdown in swirling pipe flow have only previously been compared for a Newtonian fluid[22]. It was found that the agreement was generally good between the experimental and numerical methods and so the same techniques have been utilised in this study. However, as only Newtonian fluids were considered previously, there has been no validation in this configuration of either model we employ in our simulations. In this section we compare the results from an experiment using a shear-thinning fluid and the simulations using both power-law and Carreau-Yasuda models.

A. Axial length of recirculation 'bubble'

The axial length of the recirculation bubble has been used to compare the results from experiments and numerical studies previously[22] and we do the same here, but now for a shear-thinning fluid. Figure 4 shows how the recirculation bubble increases in axial length as the Reynolds number (Re_x) is increased for a shear-thinning fluid. This is a similar trend as that found in the case

of a Newtonian fluid[22]. Figure 4 demonstrates that the power-law model provides a reasonably accurate representation of the bubble size when compared to the experimental results for xanthan gum. And, not surprisingly, the Carreau-Yasuda model provides a slightly more accurate representation of the bubble size for all Reynolds numbers. The trend of increasing length with Re_x is captured well and the downstream extent of the bubble is captured particularly well for both models.
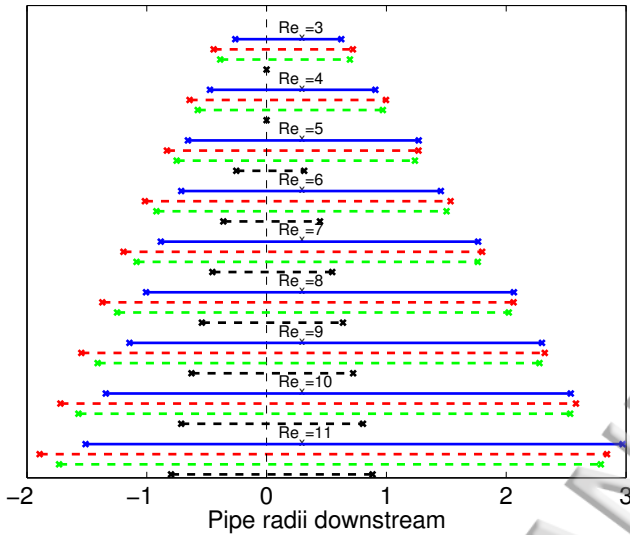

FIG. 4: Variation of recirculation bubble length with Reynolds number (Re_x) for $C_{XG} = 0.12\%$ (solid blue lines), PL 2 (dashed red lines), CY 2 (dashed green lines) and a Newtonian reference (dashed black lines). $\Gamma = 12$ in all cases.

The upstream extent of the bubble is predicted to be larger for both of the simulated models, although the Carreau-Yasuda model provides a better comparison to the experimental results than the power-law model. Because of this, it could be determined that the power-law model is over estimating the upstream extent of the bubble. However, this upstream effect is also present in the Carreau-Yasuda results and can also seen in the Newtonian results[22], so it is not solely due to the power-law model and is probably also a consequence of the visualisation technique used to determine these experimental values.

It can also be seen in figure 5 that there is a linear increase of bubble length (x_L) with Re_x in the experiments as well as both the viscosity models. The gradient is very similar in all three cases (i.e. the trend with Re_x is captured) with the difference being in the value of the absolute length of the bubble. This confirms the use of the Carreau-Yasuda model only provides a slightly more accurate representation of the length of the recirculation bubble and the power-law model is quite representative of the experimental results. For reference, the following equations (20 to 22) show the linear functions of the lines

presented in figure 5 for $Re_x > Re_c$. For $C_{XG} = 0.12$,

$$x_L = 0.44Re_x - 0.14; \qquad (20)$$

for PL2,

$$x_L = 0.43Re_x - 0.36; \qquad (21)$$

for CY2,

$$x_L = 0.43Re_x - 0.17; \qquad (22)$$

and for the Newtonian reference shown on figure 5,
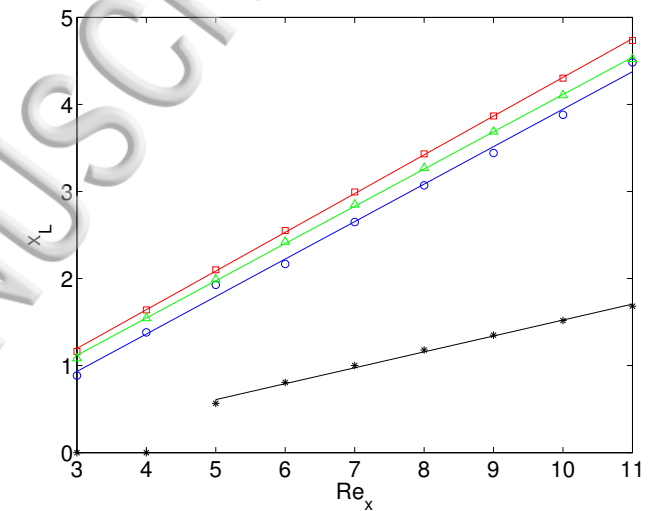
$$x_L = 0.18Re_x - 0.31. \qquad (23)$$

FIG. 5: Linear increase of recirculation bubble length (x_L) with Reynolds number (Re_x) for $C_{XG} = 0.12\%$ (blue squares), PL 2 (red circles), CY 2 (green triangles) and a Newtonian reference (black stars). Lines are linear fits to the data. $\Gamma = 12$ in all cases.

All three functions for the non-Newtonian fluid (experimental results, and power-law and Carreau-Yasuda models) are shown to have very similar gradients suggesting that all three show a similar rate of growth of the recirculation bubble with axial Reynolds number. It can also be seen that the gradient for the Newtonian reference is a lot lower. Therefore, the rate of growth of the recirculation bubble with Re_x is higher for shear-thinning fluids than Newtonian fluids. However, as will be discussed in §VI, Re_x is not the most appropriate scaling for this flow and we show these Re_x trends to compare the performance of the different viscosity models rather than any underlying physical significance.

The effect of varying the swirl ratio at a given Re_x is shown in figure 6. It is clear that both the power-law and Carreau-Yasuda models provide a reasonably good prediction of the length of the recirculation bubble and also

predict the correct trend with Γ. The Carreau-Yasuda provides results that are marginally closer to the experiments than the power-law in most cases. However, at the downstream end of the bubble this is not always true, although the differences are in fact very small.
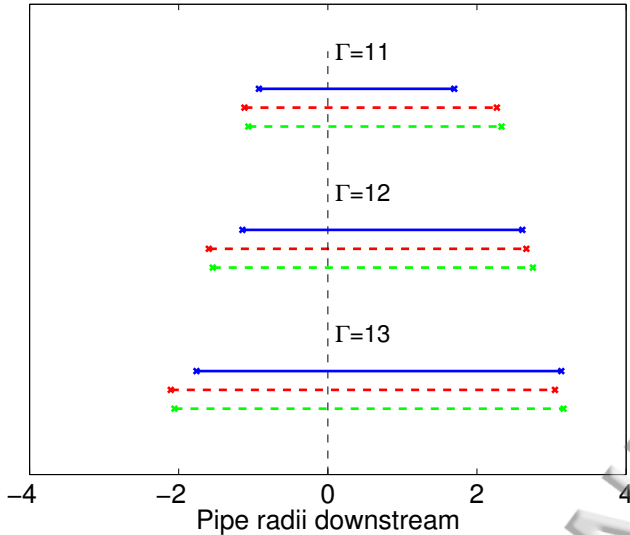

FIG. 6: Variation of recirculation bubble length with swirl ratio (Γ) for $C_{XG} = 0.15\%$ (solid blue lines), PL 3 (dashed red lines) and CY 3 (dashed green lines). $Re_x = 8$ in all cases. For this system, the critical swirl (Γ_c) = 8.53 (presented at 3 s.f.).

The effect of varying the amount of shear-thinning (or the power-law index, n) on the recirculation length is shown in figure 7 for two Reynolds numbers (Re_x). It is clear, even over this rather limited range of n, that the length of the bubble increases as the amount of shear-thinning increases (n decreases). The range of n used here is severely limited by the properties of the xanthan gum solutions it is possible to create and use in the experiment. There are no such limitation for the simulations and in §VI we numerically examine a much wider range of n. What is particularly notable in figure 7 is that for $C_{XG} = 0.15\%$ ($n = 0.46$), i.e. the most shear-thinning solution, the upstream length of the recirculation region seen in the experiment is longer than in the corresponding simulations. This is the opposite to what was seen observed at the two higher values of n (as well as figure 7). These results indicate that the variation of bubble length with shear-thinning is more dramatic in the experiment than is predicted by the simulations. This could be due to the weak effects of elasticity induced by the stagnation point here, i.e. large fluid residence times allowing significant strain to accumulate.
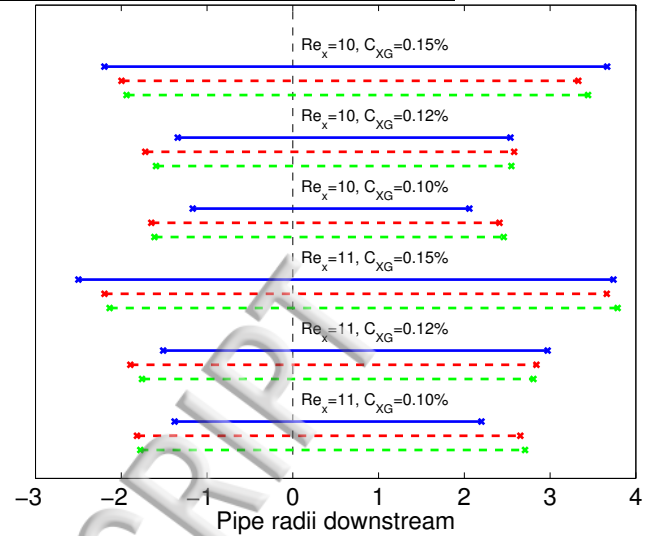

FIG. 7: Variation of recirculation bubble length with percentage of xanthan gum (solid blue lines), corresponding fitted power-law model (dashed red lines) and fitted Carreau-Yasuda model (dashed green lines). $\Gamma = 12$ in all cases.

B. Comparing power-law and Carreau-Yasuda models

Since the results above have shown that the use of the Carreau-Yasuda model has only had a minimal effect on the accuracy when representing the length of the recirculation bubble compared to the power-law model, a closer comparison was made between the two models to see how the pressure and viscosity of the flow are affected and how these properties influence each other. In figure 8 we plot the variation of viscosity along the pipe axis predicted by the Carreau-Yasuda and power-law models. For the most part it can be seen that the viscosities of the two models are in very good agreement with each other, showing very similar values. The viscosities start to deviate from each other downstream of the recirculation bubble where all power-law model viscosities increase to the maximum of 10^5 Pa.s (if this maximum had not been set the viscosities would keep increasing to infinity for all Re_x), whereas all Carreau-Yasuda model viscosities increase to an asymptote (μ_0). This shows the well-known fundamental difference between the two models with the power-law model viscosity increasing with a power law to infinity as $\dot{\gamma} \to 0$ and the Carreau-Yasuda model viscosity increasing with a power law as $\dot{\gamma}$ decreases before asymptoting to μ_0 as $\dot{\gamma} \to 0$.

The region of recirculation is marked on figure 8 and it is evident that the viscosity within the bubble is virtually identical for the two models. The large deviation is seen downstream of the vortex breakdown region where the pipe is not rotating (and the shear rate on the centreline is obviously very low). The fact that the viscosity is very similar within the bubble itself demonstrates why the

predictions of bubble length discussed previously are very similar between the two viscosity models. The main differences in viscosity are occurring outside of the region of primary interest, downstream of the vortex breakdown.
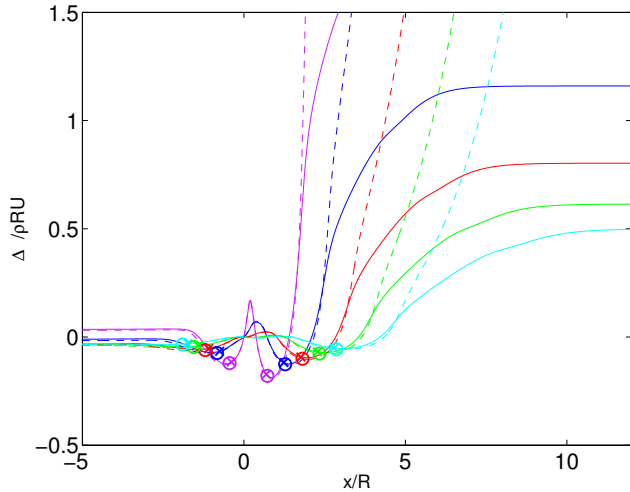

FIG. 8: The axial variation of dynamic viscosity along the pipe axis, comparing PL2 (dashed lines) and CY2 (solid lines) models for: Re_x=3 (purple), Re_x=5 (blue), Re_x=7 (red), Re_x=9 (green) and Re_x=11 (cyan), with the 'o' (PL2) and 'x' (CY2) markers show the extent of the recirculation bubble . The reference dynamic viscosity is the dynamic viscosity on the pipe axis at the join of the pipes, i.e. at $x/R = r/R = 0$. $\Gamma = 12$ in all cases.

The variance of pressure along the pipe axis and wall is shown in figures 9 and 10 respectively. It can be seen that both models produce very similar flow patterns overall. The region where the recirculation bubble occurs is where the models are in the closest agreement with each other and upstream or downstream of this region shows a slight change between the two models. At the location in the flow where the viscosities start to diverge (seen in figure 8) it is shown in figures 9 and 10 that this has no impact on the pressure difference along the pipe axis or wall. This, along with the results shown in §V A, suggests that although the use of the power-law model compared to the Carreau-Yasuda model has implications on the viscosity of the flow downstream of the recirculation bubble, this has little impact on the length of the recirculation bubble, pressure field or flow pattern as a whole.

The fact that there is no difference in the pressure fields given by the two different viscosity models is particularly important as the vortex breakdown is induced by pressure differences set up by the swirling flow. As figure 9 amply demonstrates, the pressure gradient on the axis is inverted a few radii upstream of the pipe join (due to the swirling flow) and therefore induces the backflow in this region that manifests itself as the vortex breakdown along the pipe axis. As the swirl is removed downstream
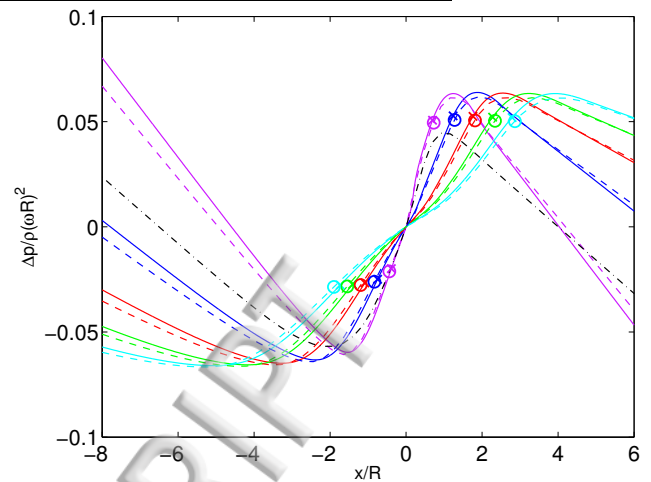

FIG. 9: The axial variation of pressure along the pipe axis, comparing a Newtonian reference line $Re_x = 7$ (black dotted and dashed line), PL2 (dashed lines) and CY2 (solid lines) models for: Re_x=3 (purple), Re_x=5 (blue), Re_x=7 (red), Re_x=9 (green) and Re_x=11 (cyan), with the 'o' (PL2) and 'x' (CY2) markers show the extent of the recirculation bubble. The reference pressure is the pressure on the pipe axis at the join of the pipes, i.e. at $x/R = r/R = 0$. $\Gamma = 12$ in all cases.

of the join the pressure gradient returns to that expected in pressure-driven constant area pipe flow and the breakdown disappears. Along the wall, figure 10 shows how the flow is accelerated around the bubble in order to compensate for the blockage effect of the recirculation region. The fact that the power-law model captures these variations in pressure gradient demonstrates why the predictions it gives are quite good for this fluid in this type of flow. It is noted that the viscosity of our experimental fluid fits a power law well over the shear rate range predominantly seen in this flow. For fluids that do not share this characteristic the above conclusions do not necessarily apply.

C. Critical swirl ratio

The critical swirl ratio (Γ_c) is defined as the lowest swirl ratio that causes a stagnation point to occur in the flow at a given Re, (i.e. the minimum swirl ratio required to induce vortex breakdown). This definition is the same as that used previously[22,23]. Figure 11 shows a comparison of the critical swirl ratio required for a 0.10% solution of xanthan gum and the corresponding numerical simulation using a power-law and Carreau-Yasuda models for viscosity. For the experiment we have included Γ_c for both "onset" and "extinction" at each Re_x. These terms are used to differentiate between when vortex breakdown is first observed as the swirl ratio is increased ("onset") and when vortex breakdown disappears as the swirl ratio
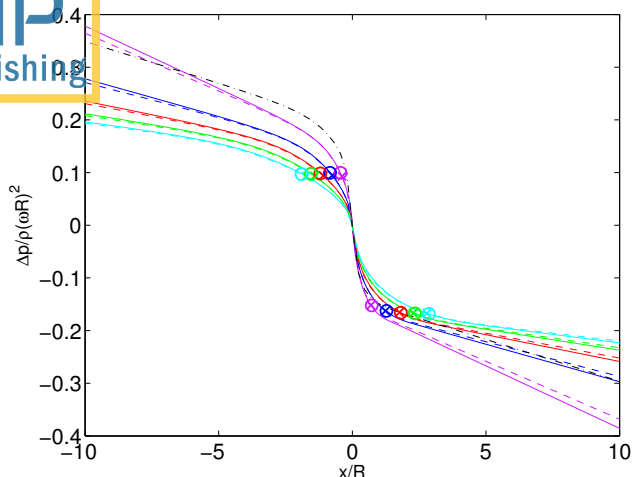
FIG. 10: The axial variation of pressure along the pipe wall, comparing a Newtonian reference line $Re_x = 7$ (black dotted and dashed line), PL2 (dashed lines) and CY2 (solid lines) models for: $Re_x=3$ (purple), $Re_x=5$ (blue), $Re_x=7$ (red), $Re_x=9$ (green) and $Re_x=11$ (cyan), with the 'o' (PL2) and 'x' (CY2) markers show the extent of the recirculation bubble. The reference pressure is the pressure on the pipe axis at the join of the pipes, i.e. at $x/R = r/R = 0$. $\Gamma = 12$ in all cases.

FIG. 11: Variation of Reynolds number (Re_x) with critical swirl ratio for experiments with 0.10% xanthan gum (shown in blue), PL 1 (red stars) and CY 1 (green crosses).

is decreased ("extinction")[22]. This is a measure of the uncertainty in visualising the vortex breakdown and is not to be taken as an indication of hysteresis (there is no hysteresis in the simulations) as previously discussed[22]. Figure 11 shows that the agreement between the experimental and numerical Γ_c is generally good for this range of Re_x as the majority of the predicted Γ_c lie within the uncertainty of the visualisation (i.e. between onset and extinction). This corresponds well (and is arguably superior) to the equivalent comparison for a Newtonian fluid[22] demonstrating that the power-law model is a good approximation to the behaviour of the xanthan gum for the purposes of predicting the swirl ratio at which breakdown will first occur.

The limited number of simulations conducted with the Carreau-Yasuda model are found to be in almost complete agreement with the power-law model (hence why we only did a limited number). This reinforces the arguments discussed above regarding the ability of the power-law model to accurately predict the pressure gradient (for the fluid studied) and this being the main driver of the vortex breakdown. It is therefore to be expected that the critical swirl ratio (effectively the critical pressure ratio) is accurately predicted.
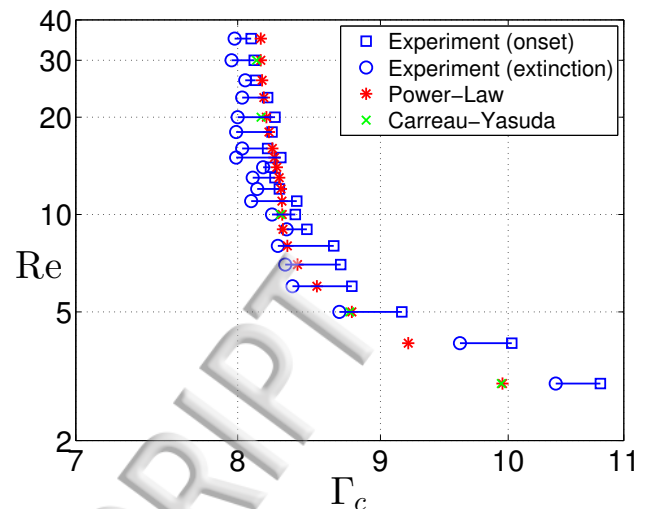
VI. THE EFFECT OF SHEAR-THINNING AND SHEAR-THICKENING

The length of the recirculation region was seen to vary with the amount of shear-thinning in figure 7. However, these results were only for a small range of shear-thinning fluids (which could be easily accessed in the experimental facility). Having shown a simple power-law model captures the experimentally observed phenomena well in section V we now present the effect of varying n_{PL} in the simulations for both power-law and simplified Carreau models over a much wider range, including shear-thickening fluids.

Figure 12 shows streamlines for a range of values of power-law index ($0.3 < n_{PL} < 1.6$) at $Re_x = 10$, $\Gamma = 12$. It is immediately obvious that the trend for the bubble length to increase with the amount of shear-thinning previously identified in figure 7 applies across this wide range of n_{PL}. As n_{PL} decreases the length of the breakdown bubble greatly increases in the axial direction, extending to several pipe radii in the most shear-thinning cases. The width of the bubble also increases, but only marginally. It is of course severely constrained by the wall of the pipe. For values of n_{PL} greater than unity, i.e. shear-thickening fluids, the size of the recirculation bubble decreases significantly when compared to the Newtonian flow. As n_{PL} is increased the recirculation bubble becomes very small and for $n_{PL} = 1.6$ in figure 12 it actually disappears, meaning breakdown does not occur for $n_{PL} = 1.6$, $Re_x = 10$ and $\Gamma = 12$.

For the Newtonian case ($n_{PL} = 1$), the power-law and simplified Carreau models are indistinguishable as is to be expected, but as the fluid becomes more shear-thinning or thickening differences between the two mod-

es become apparent. The power-law model shows an increased recirculation bubble length compared to the simplified Carreau model (with a modest $Cu_x = 1$) as the fluid becomes more shear-thinning, whereas, for the shear-thickening case the simplified Carreau model shows an increased recirculation bubble length compared to the power-law model.

It is important to note that in figure 12 we have presented results with the Reynolds number using a viscosity based on the axial shear rate (Re_x). In §IV we explained that the Reynolds number could also be defined using a viscosity based on the rotational shear rate (Re_ω). In figure 13 we present the equivalent streamlines to those in figure 12, but with constant Re_ω instead of constant Re_x. (Re_x actually varies from $Re_x = 1.756$ for $n_{PL} = 0.3$ to $Re_x = 44.41$ for $n_{PL} = 1.6$.) The large variation in the size and shape of the breakdown bubble present in figure 12 is not seen in figure 13. In fact, the flow is very similar to that of a Newtonian fluid $n_{PL} = 1$ for all values of n_{PL}. This demonstrates that the Reynolds number scaling based on rotational shear rate is perhaps a more appropriate scaling for this flow and can be used to *largely* "eliminate" the effect of shear-thinning/thickening (although some minor differences in bubble topology can be observed in figure 13). It is also apparent that when the viscosity in the Reynolds number is based on rotational shear rate there is no discernible difference between the power-law and simplified Carreau models (noting also that $Cu_\omega = 12$).

The results for only one swirl ratio are presented in figure 13. However, simulations have been conducted for further swirl ratios (up to $\Gamma = 20$, not shown) and in each case it was found that this new scaling could be used to largely eliminate the effect of the shear-varying nature of the fluid. This is a very powerful result as it allows us to predict the size and shape of the breakdown bubble for any shear-varying fluid as it will be the same across all values of n_{PL} provided that Re_ω is matched. We do note this collapse with Re_ω shown in figure 13 is not perfect and some small variation in the shape of the bubble with n_{PL} is noticeable, but when compared to the huge variation with n_{PL} seen in figure 12 the differences are minor.

A. Critical swirl ratio

The swirl ratio required to induce vortex breakdown, which was previously shown for a single power-law index (n_{PL}) in figure 11, is shown for a range of n_{PL} in figure 14. The qualitative behaviour of the critical swirl ratio is very similar across the range of n_{PL} investigated, with all appearing to approach a value of $\Gamma_c = 8$ at higher Re_x. There is a clear quantitative dependence of Γ_c on n_{PL}, with higher power-law indices requiring a higher swirl ratio to induce vortex breakdown. This dependence is not unexpected given the streamlines shown in figure 12.

As demonstrated in figure 13, the effect of n_{PL} can be

largely removed by re-scaling using a Reynolds number based on rotational shear rate (Re_ω). This re-scaling is also found to be somewhat effective for critical swirl ratio (Γ_c) as shown in figure 15. Each of the curves relating Re_ω and Γ_c are seen to broadly collapse onto a single curve (with some deviation at more extreme values of n_{PL}). This reinforces the power of this new scaling as the swirl ratio required for vortex breakdown can now be easily predicted for any shear-thinning or shear-thickening fluid. We have checked a selection of the critical swirl ratios (at the extreme n_{PL} values of 0.4 and 1.6) using the simplified Carreau model ($Cu_\omega = 12$). The results duplicate the power-law results, reinforcing the previously stated assertion that there is little variation between the power-law and simplified Carreau predictions of critical swirl ratio. Equation 24 shows a function of critical swirl ratio in terms of (Re_ω) which was found to represent the relationship reasonably well.

$$\Gamma_C = \frac{-0.64 \exp^{(-0.12 Re_\omega)}}{-0.04 Re_\omega^{0.48}} + 8. \qquad (24)$$

We also attempted to collapse the results using a Reynolds number where the viscosity is determined from a shear rate formed from a combination of the axial and rotating velocities. However, as the magnitude of the axial velocity is small compared to the rotation at the critical swirl ratio, no reasonable combination of these two components improved the collapse.

Although there is a deviation from the master curve (equation 24) at high and low values of n_{PL} the imperfect collapse is good enough that this can be used as a very simple way to predict the onset of vortex breakdown for a wide range of fluids with shear-dependent viscosity. It may therefore prove useful for designing swirling flows in which vortex breakdown is either desired or to be avoided.

VII. CONCLUSIONS

A combined numerical and experimental investigation has shown the effect of variable shear viscosity on vortex breakdown in rotating pipe flow. Experiments using a shear-thinning fluid ($0.46 < n_{PL} < 0.58$) have been conducted in order to validate the simple power-law model used for viscosity in the simulations. Agreement between the experiments and simulations is good (to within the accuracy of the experimental visualisations) for both the size of recirculation bubble and the critical swirl ratio required for the onset of vortex breakdown. A Carreau-Yasuda model was also used for the shear-thinning fluid. This showed good agreement between the experiments and the simulations but produced similar results to the power-law model simulations. Because of this there is little benefit to using the Carreau-Yasuda model over the power-law model for the shear thinning fluids and shear rates investigated here.

$Re_\omega = 2.252, n_{PL} = 1.6$

$Re_\omega = 3.701, n_{PL} = 1.4$

$Re_\omega = 6.084, n_{PL} = 1.2$

$Re_\omega = 10, n_{PL} = 1.0$

$Re_\omega = 16.44, n_{PL} = 0.8$

$Re_\omega = 27.02, n_{PL} = 0.6$

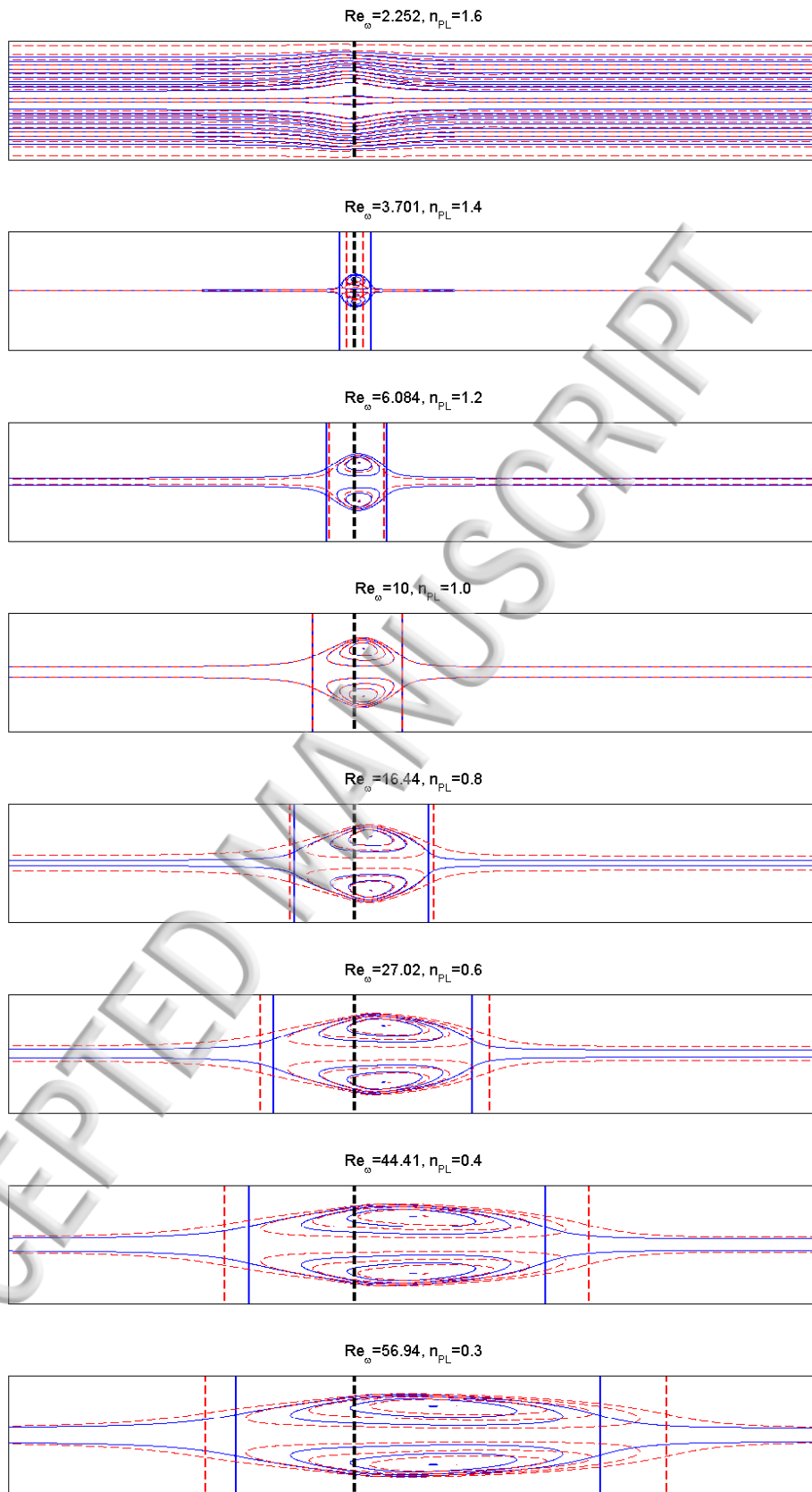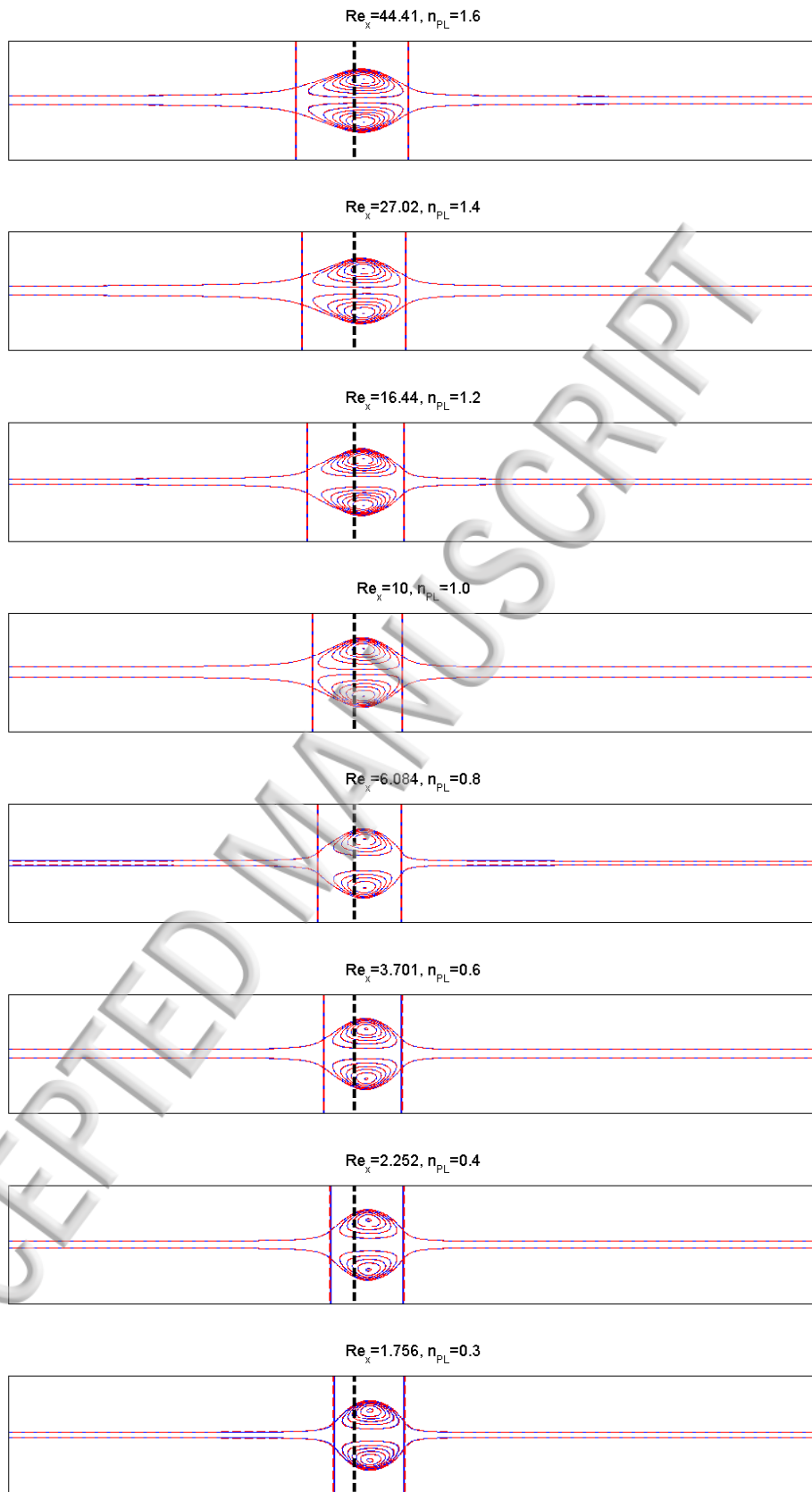$Re_\omega = 44.41, n_{PL} = 0.4$

$Re_\omega = 56.94, n_{PL} = 0.3$

FIG. 12: Streamlines showing the variation of the extent of the breakdown bubble with (n_{PL}), using power-law (dashed red lines) and simplified Carreau models (continuous blue lines), for $Re_x = 10$, $\Gamma = 12$ (and $Cu_x = 1$ for the Carreau model). The bulk flow is from left to right. The lines shown perpendicular to the bulk flow represent the axial extent of the recirculation region. For $n_{PL} = 1.6$ vortex breakdown has not occurred at this Re_x and Γ.

$Re_x=44.41, n_{PL}=1.6$

$Re_x=27.02, n_{PL}=1.4$

$Re_x=16.44, n_{PL}=1.2$

$Re_x=10, n_{PL}=1.0$

$Re_x=6.084, n_{PL}=0.8$

$Re_x=3.701, n_{PL}=0.6$

$Re_x=2.252, n_{PL}=0.4$

$Re_x=1.756, n_{PL}=0.3$

FIG. 13: Streamlines showing the variation of the extent of the breakdown bubble with (n_{PL}), using power-law (dashed red lines) and simplified Carreau models (continuous blue lines), for $Re_\omega = 10$, $\Gamma = 12$ (and $Cu_w = 12$ for the Carreau model). The bulk flow is from left to right. The lines shown perpendicular to the bulk flow represent the axial extent of the recirculation region.
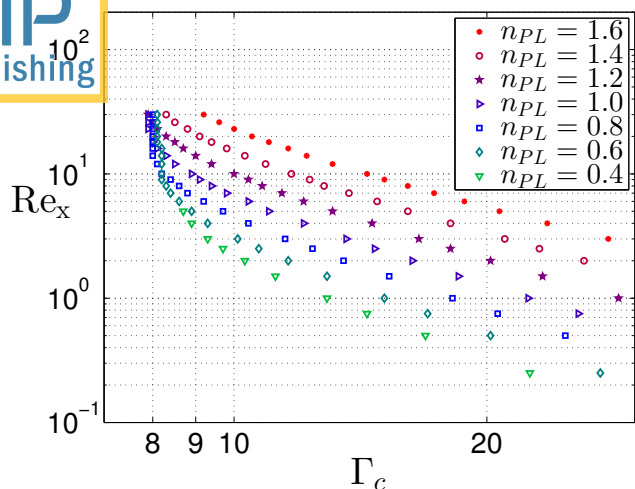
FIG. 14: Variation of Reynolds number (Re_x) with critical swirl ratio using the power-law model for power-law indices in the range 0.4–1.6.
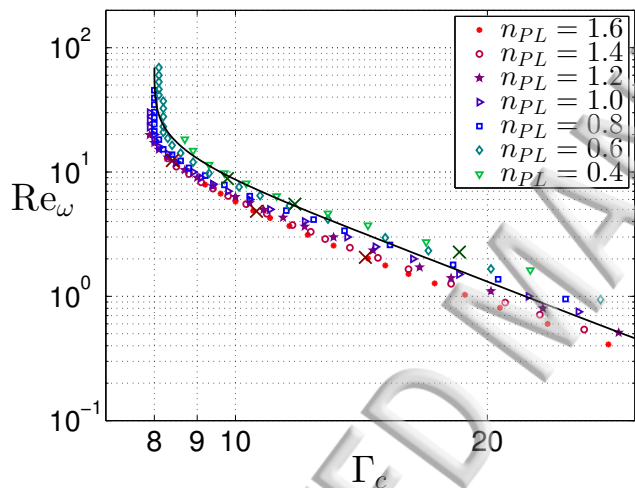

FIG. 15: Variation of Reynolds number (Re_ω) with critical swirl ratio using the power-law model for power-law indices in the range 0.4–1.6. a selection of matched simplified Carreau results are included for $n_{PL} = 1.6$ (dark red 'x' markers) and $n_{PL} = 0.4$ (dark green 'x' markers). The function shown by the equation 24 is also presented (black line).

Power-law and simplified Carreau models were used to investigate a wide range of fluids from very shear-thickening ($n_{PL} = 1.6$) to very shear-thinning ($n_{PL} = 0.3$). A new scaling is proposed using a Reynolds number with a viscosity based on a shear rate dependent on the rotational speed of the pipe (rather than the bulk flow). This scaling is found to collapse the results reasonably well across all values of n_{PL}, (i.e. shear-thinning and shear-thickening behaviour) for the critical swirl ratio and the size of the recirculation bubble, although some

subtle variation in flow topology and critical swirl ratio remains for highly shear-varying fluids. Hence, it is possible to very easily predict (with reasonable accuracy) the critical swirl ratio required to induce vortex breakdown, and the size of the recirculation bubble, for any fluid with shear-dependent viscosity.

[1] D. Peckham and S. Atkinson, *Preliminary results of low speed wind tunnel tests on a gothic wing of aspect ratio 1.0* (Royal Aircraft Establishment, 1957).

[2] S. Leibovich, "The structure of vortex breakdown," Annu. Rev. Fluid Mech. **10**, 221–246 (1978).

[3] M. Escudier, "Vortex breakdown: observations and explanations," Prog. Aerosp. Sci. **25**, 189–229 (1988).

[4] O. Lucca-Negro and T. O'Doherty, "Vortex breakdown: a review," Prog. Energy Combust. Sci. **27**, 431–481 (2001).

[5] M. Samimy, K. S. Breuer, L. Leal, and P. Steen, "A gallery of fluid motion," (2004).

[6] M. Escudier, "Observations of the flow produced in a cylindrical container by a rotating endwall," Exp. Fluids **2**, 189–196 (1984).

[7] J. Lopez and A. Perry, "Axisymmetric vortex breakdown. part 3 onset of periodic flow and chaotic advection," J. Fluid Mech. **234**, 449–471 (1992).

[8] M. R. Visbal, "Computed unsteady structure of spiral vortex breakdown on delta wings," AIAA Paper **2074** (1996).

[9] T. Hiejima, "Streamwise vortex breakdown in supersonic flows," Phys. Fluids **29**, 054102 (2017).

[10] M. Escudier and N. Zehnder, "Vortex-flow regimes," J. Fluid Mech. **115**, 105–121 (1982).

[11] J. H. Faler and S. Leibovich, "Disrupted states of vortex flow and vortex breakdown," Phys. Fluids **20**, 1385–1400 (1977).

[12] M. Escudier, "Vortex breakdown and the criterion for its occurence," in *Intense Atmospheric Vortices* (Springer, 1982) pp. 247–258.

[13] R. Goyal, B. K. Gandhi, and M. J. Cervantes, "Experimental study of mitigation of a spiral vortex breakdown at high reynolds number under an adverse pressure gradient," Phys. Fluids **29**, 104104 (2017).

[14] G. Böhme, L. Rubart, and M. Stenger, "Vortex breakdown in shear-thinning liquids: experiment and numerical simulation," J Non-Newtonian Fluid Mech **45**, 1–20 (1992).

[15] C. Day, J. Harris, J. Soria, D. Boger, and M. Welsh, "Behavior of an elastic fluid in cylindrical swirling flow," Exp. Therm Fluid Sci. **12**, 250–255 (1996).

[16] M. Escudier and L. Cullen, "Flow of a shear-thinning liquid in a cylindrical container with a rotating end wall," Exp. Therm Fluid Sci. **12**, 381–387 (1996).

[17] J. R. Stokes, L. J. Graham, N. J. Lawson, and D. V. Boger, "Swirling flow of viscoelastic fluids. part 1. interaction between inertia and elasticity," J. Fluid Mech. **429**, 67–115 (2001).

[18] J. R. Stokes, L. J. Graham, N. J. Lawson, and D. V. Boger, "Swirling flow of viscoelastic fluids. part 2. elastic effects," J. Fluid Mech. **429**, 117–153 (2001).

[19] Z. Rusak and J. A. Tichy, "Near-critical swirling flow of viscoelastic fluids in a pipe," in *ASME 2002 Joint US-European Fluids Engineering Division Conference* (American Society of Mechanical Engineers, 2002) pp. 1261–1268.

[20] P. Bar-Yoseph and Y. Kryzhanovski, "Axisymmetric vortex breakdown for generalized newtonian fluid contained between rotating spheres," J Non-Newtonian Fluid Mech **66**, 145–168 (1996).

[21] C. Palacios-Morales and R. Zenit, "The formation of vortex rings in shear-thinning liquids," J. Non-Newtonian Fluid Mech. **194**, 1–13 (2013).

[22] D. J. Dennis, C. Seraudie, and R. J. Poole, "Controlling vortex breakdown in swirling pipe flows: experiments and simulations," Phys. Fluids **26**, 053602 (2014).

[23] Z. Lavan, H. Nielsen, and A. Fejer, "Separation and flow reversal

in swirling flows in circular ducts," Phys. Fluids **12**, 1747–1757 (1969).

[24]H. McDonald, "The zeros of $j\_1^2(\zeta)$-$j\_0(\zeta)j\_2(\zeta)$=0 with an application to swirling flow in a tube," SIAM J. Appl. Math. **51**, 40–48 (1991).

[25]C. Crane and D. Burley, "Numerical studies of laminar flow in ducts and pipes," J. Comput. Appl. Math. **2**, 95–111 (1976).

[26]D. Silvester, R. Thatcher, and J. Duthie, "The specification and numerical solution of a benchmark swirling laminar flow problem," Computers & fluids **12**, 281–292 (1984).

[27]S. Wang and Z. Rusak, "The dynamics of a swirling flow in a pipe and transition to axisymmetric vortex breakdown," J. Fluid Mech. **340**, 177–223 (1997).

[28]Z. Rusak, S. Wang, and C. Whiting, "The evolution of a perturbed vortex in a pipe to axisymmetric vortex breakdown," J. Fluid Mech. **366**, 211–237 (1998).

[29]S. Rafaï, D. Bonn, and A. Boudaoud, "Spreading of non-newtonian fluids on hydrophilic surfaces," J. Fluid Mech. **513**, 77–85 (2004).

[30]D. A. Gagnon, N. C. Keim, and P. E. Arratia, "Undulatory swimming in shear-thinning fluids: experiments with caenorhabditis elegans," J. Fluid Mech. **758** (2014).

[31]A. S. Haase, J. A. Wood, L. M. Sprakel, and R. G. Lammertink, "Inelastic non-newtonian flow over heterogeneously slippery surfaces," Phys. Rev. E **95**, 023105 (2017).

[32]E. Chiarello, A. Gupta, G. Mistura, M. Sbragaglia, and M. Pierno, "Droplet breakup driven by shear thinning solutions in a microfluidic t-junction," Phys. Rev. Fluids **2**, 123602 (2017).

[33]M. Escudier, I. Gouldson, A. Pereira, F. Pinho, and R. Poole, "On the reproducibility of the rheology of shear-thinning liquids," J. Non-Newtonian Fluid Mech. **97**, 99–124 (2001).

[34]H. M. A. Dakhil, *A narrow-gap rotational rheometer for high shear rates and biorheological studies*, Ph.D. thesis, Friedrich-Alexander-Universitt Erlangen-Nrnberg (2016).

[35]R. Poole and B. Ridley, "Development-length requirements for fully developed laminar pipe flow of inelastic non-newtonian liquids," J. Fluids Eng. **129**, 1281–1287 (2007).

[36]M. Escudier, P. Oliveira, F. Pinho, and S. Smith, "Fully developed laminar flow of non-newtonian liquids through annuli: comparison of numerical calculations with experiments," Exp Fluids **33**, 101–111 (2002).